Assessment of qualitative and quantitative S 0 guided wave tomography of sharp thickness loss defects in the isotropic membrane regime

William Cailly, Henri Walaszek, Sébastien Brzuchacz, Fan Zhang, Philippe Lasaygues

Assessment of Qualitative and Quantitative S_0 Guided Wave Tomography of Sharp Thickness Loss Defects in the Isotropic Membrane Regime

William Cailly,[1, a] Henri Walaszek,[2] Sébastien Brzuchacz,[2] Fan Zhang,[2] and Philippe Lasaygues[1]

[1] *Aix-Marseille University, CNRS, Centrale Marseille, Laboratoire de Mécanique et d'Acoustique, 4 impasse Nikola Tesla, 13013 Marseille, France.*

[2] *Technical Center for Mechanical Industry, CETIM, 52 Avenue Flix Louat, 60300 Senlis, France.*

(Dated: 28 January 2021)

Progress in instrumentation, computer hardware and inversion methods is encouraging the development of more advanced guided wave tomography techniques, especially for Nondestructive Testing (NDT) of plate structures to characterize corrosion. An experimental S_0 tomography performance assessment in the membrane regime is reported. One of the main interests of the fundamental membrane regime is that in this regime waves are propagated over long distances. A 2 mm thick steel disk containing calibrated sharp artificial defects (flat bottom holes) is tested in both reflection and extinction modes. A reconstruction algorithm derived from the membrane approximation is presented. We expose a complete reflection mode inversion approach which includes beam inversion, waveform deconvolution and thickness loss calibration. Non-linear correction factors are introduced and discussed for quantitative imaging. A width-regularity-depth description of defects is introduced to put the results into persepective with other defect geometries. The results show the relevance of the inversion method to enhance the imaging performance with regard to defect localization and sizing. Crucial points concerning instrumentation such as coupling, signal-to-noise ratio, excitation mode, coupling, selection of frequency, are also discussed.

[a]cailly@lma.cnrs-mrs.fr

I. INTRODUCTION

A. Context and purpose

Guided wave tomography (GWT) is an imaging technique that makes it possible to reconstruct variations in the geometry or in the acoustical properties of a waveguide from diffraction or time-of-flight data. The major purpose of GWT is the Nondestructive Testing (NDT) of plate structures to characterize corrosion. This issue concerns various fields of industry such as mechanical industry, aircraft industry, petrochemical industry, energy. One can classify the characterization of corrosion into three stages: (i) detection, (ii) localization and significance assessment, and (iii) quantitative reconstruction of thickness map. Advances in recent years have shown the relevance of qualitative algorithms to localize defects in plates (Albiruni *et al.*, 2012; Huang *et al.*, 2016; Wang *et al.*, 2016). Algorithms such as the RAPID algorithm (Reconstruction Algorithm for the Probabilistic Inspection of Damage) provide simplified, easy-to-implement reconstruction methods allowing a fast representation of the defects (Tabatabaeipour *et al.*, 2014; Wang *et al.*, 2010). Today, progress in instrumentation, hardware and inversion methods is encouraging the development of more advanced GWT techniques. The assessment of the performance of quantitative thickness imaging techniques is now under investigation. Particular notice should be taken in this context of the HARBUT algorithm (Hybrid Algorithm for Robust Breast Ultrasound Tomography), developed by P. Huthwaite and F. Simonetti, and applied to quantitative thickness A_0 mode tomography (Huthwaite and Simonetti, 2011, 2013). Recently, the application of this algorithm to passive corrosion monitoring showed good results (Druet *et al.*, 2019). The advantages of GWT for

NDT has been widely exposed in the literature. One can note that recent works dealt with the possibilities of high resolution imaging of defects in plates using electrical impedance tomography (Nonn *et al.*, 2018; Zhao *et al.*, 2015; Zhao and Semperlotti , 2019). Against this background, the work reported here, which focuses on the fundamental case of low-frequency S_0 mode tomography, aims to contribute to the development of advanced GWT techniques.

B. Problem and content

In a previous paper, the present authors dealt with issues related to GWT of isotropic plates, such as the validity of different approximations (first Born approximation, mode conversion neglect, high order mode neglect), the possibility of quantitative reconstruction of deep defects, the methodology for thickness reconstruction algorithm implementation (Cailly *et al.*, 2019). In that study, we chose a 1D quantitative formalism based on the Mindlin-Reissner theory and Born series theory, see (Mindlin, 1951; Reissner, 1945; Rose and Wang, 2004), to propose a description of direct and inverse guided wave diffraction by thickness loss defects. This formalism is easily extended to the 2D case to include shear-SH–compression-S–flexural-A mode conversion and 2D directivity effects. Building on that previous work, an experimental S_0 tomography assessment was carried out. One of the main advantages and interest of low-frequency S_0 testing is the possibility of propagation over long distances.

The experimental setup we chose is similar to the setup used by M. Lowe and O. Diligent to study the 1D S_0 diffraction by thickness loss defects (Lowe and Diligent, 2002). To extend Lowe's experiment to a 2D case, and to perform image reconstruction, we tested

a disk containing flat bottom holes, in both reflection mode and extinction mode. The selection of defects under study plays an important role. It is known that the diffraction by defects in plates is very dependent on the defect geometry. A width-regularity-depth analysis of defects was proposed by P. Huthwaite (Huthwaite, 2014). This elementary representation is very useful to characterize a defect and to select the reconstruction algorithm hypotheses. Significant research was carried out in the field of guided wave diffraction in plates by the group of M. Lowe and P. Cawley. In particular, they contribute to the understanding of guided wave diffraction by circular defects in plates (Diligent *et al.*, 2002, 2003). Although obtained for flat bottom hole defects, the results presented here can be put into perspective with the results obtained for other defect geometries using the representation proposed by P. Huthwaite. To achieve this, predictions of diffraction by defects were computed in the depth-width-regularity space, after having introduced the membrane approximation. The exposition of the methodology, as well as that of the results, is presented in two sections: in the case of reflection mode and in the case of extinction mode. These two well-known imaging configurations are intrinsically distinct. One or the other of these configurations can be encountered in practice. Finally, a synthetic examination of the proposed imaging performance is discussed.

II. GLOBAL METHODOLOGY

A. The membrane model approximation

Considering an infinite isotropic plate of density ρ, thickness h and elasticity constants E and ν, the linear first-order shear approximation neglecting lateral contraction and out-of-plane displacement leads to the following Helmholtz equation involving the in-plane displacement $\mathbf{u}$, for a given angular frequency ω:

$$I_0(\mathbf{x})\rho\omega^2\mathbf{u}(\mathbf{x}) + \mathrm{div}\left(I_0(\mathbf{x})\boldsymbol{c} : \nabla\mathbf{u}(\mathbf{x})\right) = \mathbf{0}\,, \tag{1}$$

where $\boldsymbol{c}$ denotes the isotropic elasticity constant tensor, under the plane stress hypothesis, and I_0 denotes the space-dependent (variable $\mathbf{x}$) zeroth order plate moment, which is identified with the plate thickness h. A defect is supposed to be a localized perturbation δI_0 of a constant nominal thickness I_0.

$$I_0(\mathbf{x}) = I_0 + \delta I_0(\mathbf{x})\,. \tag{2}$$

The validity of the membrane approximation has been discussed in our previous work (Cailly *et al.*, 2019). Two modes are described: S_0 and SH_0. It is known that the membrane approximation is relevant in the low frequency range for which the S_0 is not dispersive, whose speed corresponds to the pressure-membrane wave speed c_M. The fundamental shear mode SH_0 propagates at shear wave speed c_S. The part of diffracted energy in the A_0 and A_1 modes is neglected. Consequently, it is expected that the reconstructed defects in the membrane approximation are oversized. The authors showed that this approximation

is relevant for thickness loss up to about 50 % of the nominal thickness. We noted that the complete 2D Mindlin-Reissner model, which includes six modes, may be too complex to tackle the definition and the implementation of a tomography algorithm for the case under study. Using the following Helmholtz decomposition of $\mathbf{u}$:

$$\mathbf{u} = \nabla\phi + \nabla \times \mathbf{H}\,, \tag{3}$$

the following formalism is used to describe a solution of equation (1) written in terms of a vector $\mathbf{d} := [\phi, H_z]^T$:

$$\mathbf{d}(\mathbf{x}, \omega) = \sum_{n=1}^{2} \int_{S^1} a_n(\mathbf{s}) e^{ik_n(\omega)\mathbf{s}\cdot\mathbf{x}} \mathbf{e}_n d\mathbf{s}\,, \tag{4}$$

where S_1 denotes the unit circle. The variable $a_n(\mathbf{s})$ denotes a particular plane wave spectrum. Taking index 1 for S_0 mode and 2 for SH_0 mode we have:

$$k_1^2(\omega) = \frac{\rho\omega^2}{E'}, k_2^2(\omega) = \frac{\rho\omega^2}{\mu}\,, \tag{5}$$

where E' denotes the plane stress modified Young modulus, and

$$\mathbf{e}_1 = [\phi, 0]^T, \mathbf{e}_2 = [0, H_z]^T\,. \tag{6}$$

Using this formalism, the diffraction transfer function, associated with a thickness perturbation δI_0, relating a given incident field of spectrum b, at an angle of incidence $\mathbf{s}_0$, to the scattered field of spectrum a is expressed, in tensorial form, by

$$a_n(\mathbf{s},\omega) = t_n^m(\mathbf{s},\mathbf{s}_0,\omega,\delta I_0) b_m(\mathbf{s}_0,\omega)\,. \tag{7}$$

Applying the first Born approximation, one can derive the linear diffraction coefficients $t_n^m(\mathbf{s},\mathbf{s}_0,\omega,\delta I_0)$ that are given in appendix A.

B. Prediction of the diffraction behavior by elementary defects

The diffraction/scattering behavior of a localized thickness perturbation is strongly dependent on the ratio between its characteristic size d and the wavelength λ of the incident wave. The analytical membrane model makes it possible to get a simple approximated global prediction of 2D thickness loss defect diffraction behavior in the diameter-regularity-depth space. A possible geometric representation of a defect is as follows. One can define the generalized Gaussian profile, depending on the radial variable r, with 3 parameters $d, \beta, \delta h$, by:

$$\delta h_{d,\beta,\delta h}(r) := \delta h e^{-(2/d)^\beta \ln(2)|r|^\beta}\,. \tag{8}$$

The diameter of the profile d is defined at $\delta h/2$. The β parameter describes the regularity of the profile. For convenience, one can also define:

$$\alpha := 2/\beta\,. \tag{9}$$

The most regular case corresponds to $\beta = 2$, $\alpha = 1$ (Gaussian) and has the property of not having secondary lobes in the frequency domain. In the least regular case, $\beta = \infty$, $\alpha = 0$, the profile is rectangular. By using this representation we give the diffraction diagrams for axisymmetric defects in terms of the three parameters: diameter (d), depth ($\delta h/h$) and regularity (β). The diagrams were calculated using a 2D-FFT Born series method with 16 terms under the membrane hypothesis. We chose the following time domain diffraction/scattering quantity:

$$\text{Scattered Amplitude}_n^m(\mathbf{s}, d) := \frac{\max(s(t) * t_n^m(\mathbf{s}, t, d))}{\max(s(t))}\,, \tag{10}$$

where s denotes a broadband signal centered around a given frequency. The axes d/λ in the time domain diagrams are given with respect to this center frequency.

The diagrams in figures 1 and 2 illustrate the effects of regularity and depth on the diffraction. The first resonance of the defect occurs at a fraction of the wavelength, between 0.25λ and 0.4λ, depending on the definition of d. The diffraction/scattering energy of a defect is strongly dependent on its regularity. The regular defects are transparent at high frequencies. An interesting property of the Gaussian defect is that it has only one lobe, associated with the fundamental resonant frequency. Figure 1 illustrates the influence of the regularity and the difference in behavior between the reflection and extinction responses to a broadband pulse. Figure 2 illustrates the non-linearity of the defect response with the defect thickness loss. This method may be useful to predict the detectability of a defect of a given geometry.

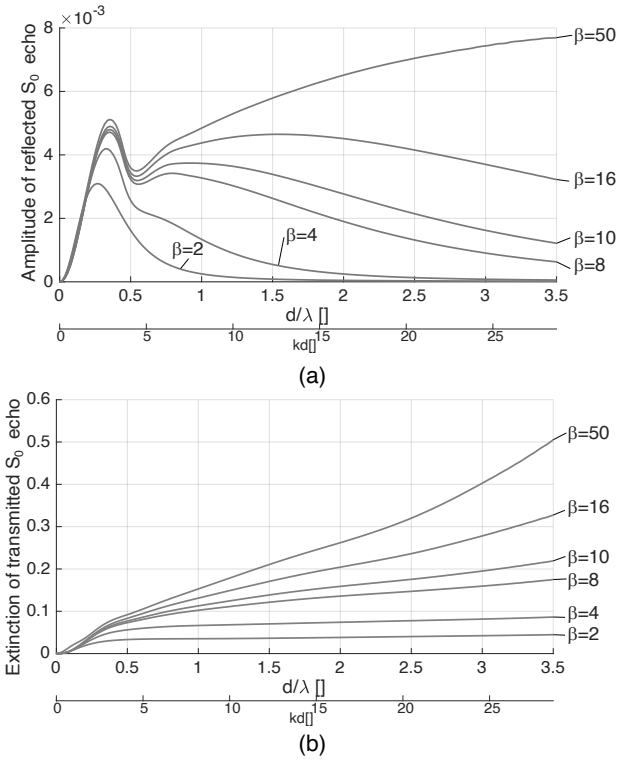

FIG. 1. Diagrams of membrane compression wave (S_0) diffraction/scattering by thickness loss defects of depth -10% for different regularity parameters β, in the time domain for a Gaussian waveform of envelope width at -6 dB of 1.25×the central period: (a) $S_0 \to S_0$ reflection, (b) $S_0 \to S_0$ extinction.

C. Definition of the experimental phantom

The tested phantom consisted of a steel disk, diameter 320 mm and thickness 2 mm, containing artificial sharp defects (flat bottom holes). The measurement of the acoustic properties of the phantom's material is given in appendix B 1. The drawing of the phantom is given in figure 3. The defects were arranged in a spiral in an area not too far from the center. The diameters and depths of the phantom defects were chosen according to the criterion of the reflected echo amplitude defined in the previous paragraph (eq. (10)). Thus,

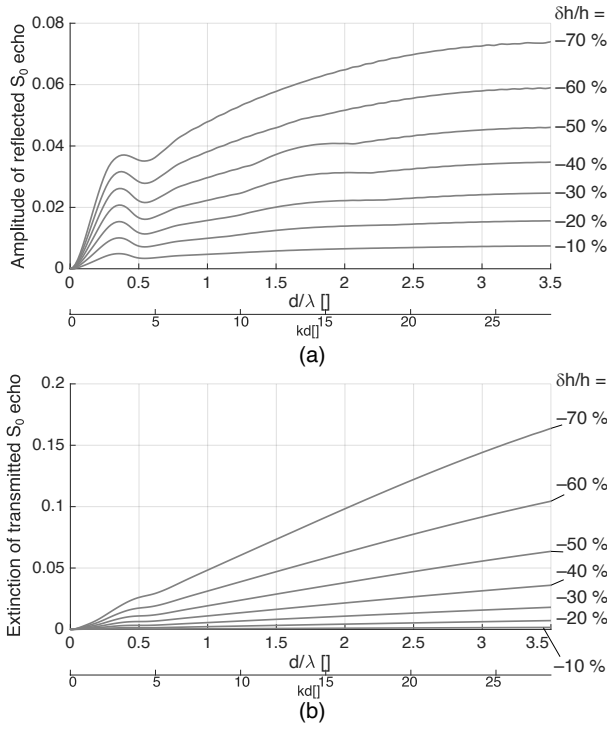

FIG. 2. Diagrams of membrane compression wave (S_0) diffraction/scattering by thickness loss defects of regularity parameter $\beta = 50$ for different depths, the time domain for a -6 dB envelope width Gaussian waveform of 1.25×the central period: (a) $S_0 \to S_0$ reflection, (b) $S_0 \to S_0$ extinction.

depth and diameter of the defects were chosen so that they had the same order of magnitude of in terms of reflected amplitude. The comparison in normalized scale of the estimated scattering diagrams of the defects is given in figure 4. These results were calculated using the membrane approximation Born series method for a waveform with center frequency $f_c = 500$ kHz and bandwidth at -6 dB $\approx 0.7 f_c$. According to these estimations, the three defects have approximately the same reflectivity behavior (left part of the diagram). They

do not have the same extinction amplitude and aperture (right part of the diagram). This will be discussed in the extinction tomography section.

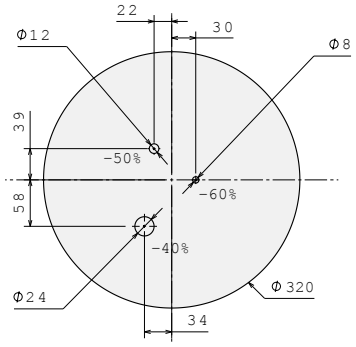

FIG. 3. Geometry of the phantom disk with a diameter of 320 mm and a thickness of 2 mm with three thickness loss defects; the depth of defects is indicated in the figure (percentage of nominal thickness).

III. REFLECTION MODE METHODOLOGY

A. Experimental setup

Building on the principle of the experimental configuration developed by M. Lowe and O. Diligent (Lowe and Diligent, 2002), the reflection mode experiment consisted in exciting the edge of the disk by a PANAMETRICS^{TM} 500 kHz 1 inch aperture single-element contact transducer. The coupling was performed using a conventional coupling gel. The authors reported in their article that coupling was made difficult by the smallness of the excitation surface. The transducer was kept fixed. Insonification at different angles was performed by manually rotating the disk. At each angular position, we minimized the inhomogeneity of

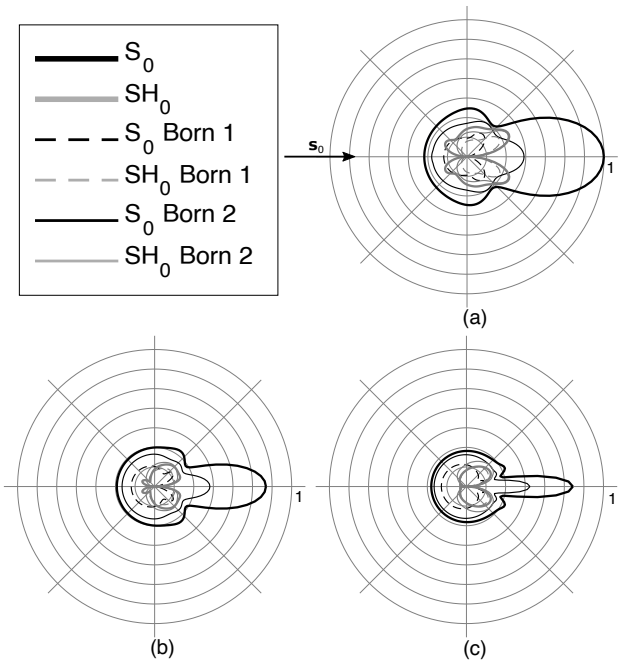

FIG. 4. Estimation of the far-field directivity diagrams of phantom's defects insonified by a plane wave S_0 with center frequency $f_c = 500$ kHz and bandwidth at -6 dB $\approx 0.7 f_c$, in normalized scale, by the method of Born series, showing first (Born 1) and second (Born 2) Born approximations,: a. $d = 8$ mm 60 % deep, b. $d = 12$ mm 50 % deep, c. $d = 24$ mm 40 % deep.

the coupling by doing the same coupling application operation. Nevertheless, we expected some amplitude variations due to the inhomogeneity of the coupling. The angular step chosen was 5 degrees, thus 72 positions were performed. The photograph of the reflection mode experimental setup is given in figure 5.

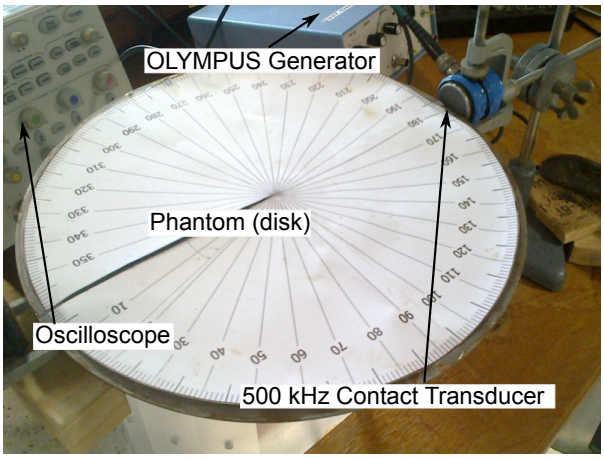

FIG. 5. Photograph of the reflection mode experimental setup.

B. Reconstruction algorithm

1. 2D Radon inversion formula

Let us expose the reflection mode thickness reconstruction algorithm derived from the membrane approximation. The first Born far field diffraction coefficient formula t_1^1 is given in appendix A in equation (A1). We rewrite this equation in the time domain and in the case of pure reflection, *i.e.* $\mathbf{s} = -\mathbf{s}_0$:

$$t_1^1(\mathbf{s}_0, t) = C(t) * \frac{1}{I_0}\mathbf{s}_0 \cdot \int_{\mathbb{R}^2} \nabla \delta I_0(\mathbf{x}) \delta \left(t - \frac{2\mathbf{s}_0 \cdot \mathbf{x}}{c_M} \right) d\mathbf{x}\,, \tag{11}$$

where $C(t)$ denotes the 2D far field decreasing function, which depends on the observation distance and c_M. The linear direct diffraction problem is rewritten in the time domain:

$$a(\mathbf{s}_0, t) = t_1^1(\mathbf{s}_0, t) * b(t)\,, \tag{12}$$

where a and b are the diffracted and incident S_0 mode signals, respectively. By integrating, for each angle, the quantity $\mathbf{s}_0 \cdot \nabla \delta I_0 = \partial_{\mathbf{s}_0} \delta I_0$ along the variable $r = \mathbf{s}_0 \cdot \mathbf{x}$, and by noticing that $dr = dt c_M/2$, one can obtain the Radon-type inversion formula:

$$\delta I_0(\mathbf{x}) = \frac{I_0}{4\pi} \int_{S^1} \int_{\mathbb{R}} \int_{-\infty}^{t} \frac{c_M}{2} \check{a}(\mathbf{s}_0, t') dt' * \acute{\delta} \left(t - \frac{2\mathbf{s}_0 \cdot \mathbf{x}}{c_M} \right) dt d\mathbf{s}_0 \,, \tag{13}$$

where

$$\check{a}(\mathbf{s}_0, t) := b^{-1}(t) * C^{-1}(t) * a(\mathbf{s}_0, t) \tag{14}$$

denotes the deconvolved sinogram, and $\acute{\delta}$ denotes the ramp-filtered version of Dirac distribution δ. Using commutativity of the application of the kernel $\acute{\delta}$ and of the integration in t', one can rewrite this inversion formula:

$$\delta I_0(\mathbf{x}) = \frac{I_0}{4\pi} \frac{c_M}{2} \int_{S^1} \int_{\mathbb{R}} \check{a}(\mathbf{s}_0, t) * \acute{H} \left(t - \frac{2\mathbf{s}_0 \cdot \mathbf{x}}{c_M} \right) dt d\mathbf{s}_0 \,, \tag{15}$$

where $\acute{H}$ is the ramp-filtered Heaviside kernel defined by

$$\acute{H}(r) := \int_{-\infty}^{r} \acute{\delta}(r') dr' \tag{16}$$

$$\acute{\delta}(r) := \frac{1}{2\pi} \int_{\mathbb{R}} |k| e^{ikr} dk \,. \tag{17}$$

2. Selection of the deconvolution algorithm

Quantitative thickness reconstruction requires the deconvolution of the measured sinogram, see eq.(14). The deconvolution process involves two inverse filters: (i) the decon-

volution by the waveform of the acoustic excitation, also including the linear response of the device measuring the electrical signal, denoted by b^{-1}, and (ii) the compensation of the natural decrease due to 2D propagation in the plane of the plate, denoted by C^{-1}. The decrease law was determined empirically using the multiple echo method. A power law $A(t) = A_0(t/t_0)^p$ was fitted. We measured for the disk case: $A_0 = 5684.5$ mV, $p = -0.54$, where $t_0 = 1$ μs, and t expressed in μs. The Time Gain Compensation (TGC) law A^{-1} was applied to the sinogram. The interest of the TGC is that it enhances the echoes coming from the propagation over long distances. The inspected area is not too large relative to the wavelength, so we noticed that the effect of TGC was relatively weak.

The inversion of the measurement system implies the inversion of the waveform. The normalized measured waveform of the transducer is given in figure 6. The chosen deconvolution algorithm was a gradient descent of a quadratic functional f with l_p-norm penalization:

$$f(x) = ||a - x * b||_2^2 + \lambda^p ||x||_p^p \tag{18}$$

$$x_{n+1} = x_n - \alpha_k \partial_x f \tag{19}$$

$$x_0 = a\,, \tag{20}$$

where x denotes the deconvolved signal and a the observed signal. The penalization constant λ was adjusted empirically from the Signal-to-Noise Ratio (SNR) measurement. Because of the sharpness of the selected defects, we assumed a sparse representation of the signals. The sparsity is determined by the selection of l_p. We set p =1 and varied the penalty parameter λ. The sparse deconvolution methods are relevant for the case of signals composed of localized

echoes, in particular in Ultrasonic Testing (Bossmann *et al.*, 2012; Carcreff *et al.*, 2015; O'Brien *et al.*, 1995; Soussen *et al.*, 2012; Zala, 1992). The interest of the deconvolution methods for ultrasound computed tomography is known (Lasaygues and Lefebvre, 2000).

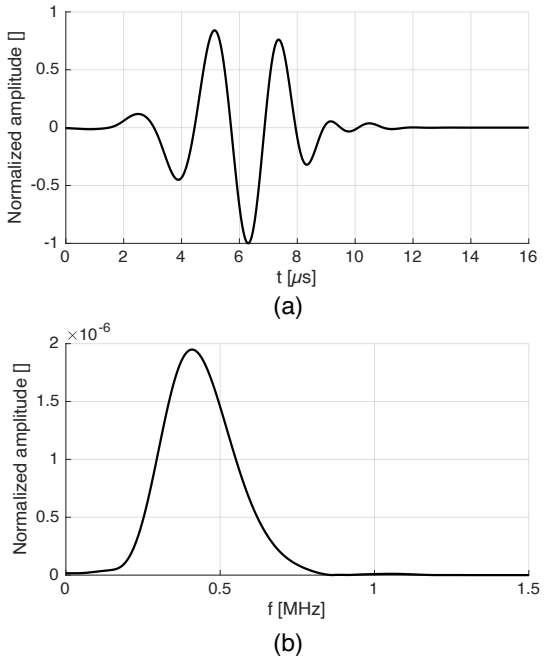

FIG. 6. Measured waveform of the 500 kHz contact transducer: (a) time domain, (b) frequency domain.

The sparse representation is exact for 1D defects of rectangular profile but is not valid in the case of 2D flat bottom hole defects because of the 2D diffraction components outside the insonification axis. On the one hand, the sparse deconvolved signal gives rise to very strong gradients, which are not consistent with the actual defect. But on the other hand, the sparse representation is relevant, even necessary, for the best localization of the defects. Consequently, we made the following assumption: there exists a low-pass filter (LP) that limits the high-frequency effects of 2D reconstruction applied to a sparse representation while

maximizing the localization of information. This filter therefore requires prior knowledge about the regularity and the size of the defects. The LP filter was adjusted empirically. The estimation of the linear response to the thickness loss was performed empirically by using a calibration plate containing flat bottom holes of different depths. Details of the adjustment of the deconvolution process are given in appendix B 2.

3. Adjoint FEM tomography

A finite element method (FEM) model of the disk was developed in order to predict the direct field and to compute the adjoint fields associated with the phantom's defects. The model considered was the 2D membrane model given in equation (1). We chose linear quadrangle elements Q_1 with an average size of 0.6 mm. The parameters of the model (material constants, source waveform, conversion coefficient from simulation to electric signals given in mV) were fit according to the measurements made on a healthy disk of same size and material. The excitation was modeled by a radial force applied to the edge of the disk, on an aperture of 10 mm. The transducer was not modeled. Details showing the fit of the FEM model are given in appendix B 3. The selected adjoint field tomography algorithm was based on the quadratic cost functional χ, which depends on the thickness I_0, defined for a given insonification angle $\mathbf{s}_0$ by:

$$\chi(I_0, \mathbf{s}_0) := \int_0^T \left(u_{syn}(t, \mathbf{s}_0) - u_{obs}(t, I_0, \mathbf{s}_0)\right)^2 dt\,, \tag{21}$$

where u_{syn} and u_{obs} denote the direct and observed fields (at the edge of the disk, in the radial direction), respectively. By applying the Fréchet derivative method, see *e.g.* (Liu and

Tromp, 2008), one can show that, from the direct model, in equation (1) rewritten in the time domain, the variation of the functional for a perturbation in thickness is:

$$\delta\chi/\delta I_0(\mathbf{s}_0) = \int_\Omega K_{I_0}(\mathbf{x}, \mathbf{s}_0) d\mathbf{x}\,, \tag{22}$$

$$\begin{aligned} K_{I_0} = -\int_0^T & \underbrace{(\rho u_{adj}(T-t)\partial_{tt} u_{syn}(t)}_{\text{density perturbation}} \\ & - \underbrace{u_{adj}(T-t)\mathrm{div}(c : \nabla u_{syn}(t))}_{\text{stiffness perturbation}}\, dt\,, \end{aligned} \tag{23}$$

where Ω denotes the 2D disk. The dependencies on $\mathbf{x}$ and $\mathbf{s}_0$ are implicit in the expression of the kernels K_{I_0}. The thickness perturbation kernels K_{I_0} involve a density perturbation component and a stiffness perturbation component. The adjoint field u_{adj} is the backpropagation of the residue, identified with the observed signal containing the echoes coming from the defects, for a given angle. The fields u_{adj} and u_{syn} are obtained by FEM. We thus have a qualitative tomography of the perturbation of thickness of the form:

$$f(\mathbf{x}) = \frac{1}{2\pi} \int_{S^1} K_{I_0}(\mathbf{x}, \mathbf{s}_0) d\mathbf{s}_0\,. \tag{24}$$

4. Secant method for quantitative imaging

As shown in figure 2, the reflection amplitude of a defect is non-linear with respect to defect depth. The secant method, discussed in our cited previous work, was tested to perform

non-linear inversion. We defined the functional J which depends on the thickness contrast perturbation $\delta\mathrm{h} := \delta h/h \in [0,1]$:

$$J(\delta\mathrm{h}) = \text{Born inv}(a) - \text{Born inv}\left(F(\delta\mathrm{h})\right) , \tag{25}$$

where Born inv$(\cdot)$ denotes the thickness contrast obtained by the linear Born inversion operation on a given sinogram, see equation (15), a denotes the measured sinogram, and $F(\delta\mathrm{h})$ the computed sinogram from the direct problem applying the thickness map $\delta\mathrm{h}$. The direct problem was solved using the FEM method. The numerical sinogram obtained was then normalized using the adjustment of the direct problem to the healthy disk measurements as described above. The secant iterative algorithm for finding the zero of J is:

$$\delta\mathrm{h}_{j+1} = \delta\mathrm{h}_j - \frac{\delta\mathrm{h}_j - \delta\mathrm{h}_{j-1}}{J(\delta\mathrm{h}_j) - J(\delta\mathrm{h}_{j-1})} J(\delta\mathrm{h}_j)\,. \tag{26}$$

We computed only the first secant $\delta\mathrm{h}_2$, the global convergence behavior of the secant being known. Taking $\delta\mathrm{h}_0 = 0$ and $\delta\mathrm{h}_1 = \text{Born inv}(a)$, one can get, for a small parameter ϵ:

$$\delta\mathrm{h}_2 = \delta\mathrm{h}_1 \underbrace{\frac{\delta\mathrm{h}_1}{\text{Born inv}(F(\delta\mathrm{h}_1)) + \epsilon}}_{\text{first secant correction}} . \tag{27}$$

We compared the first secant result $\delta\mathrm{h}_2$, which includes 2D effects and the $S \leftrightarrow SH$ mode conversion in the $F(\delta\mathrm{h}_1)$ computation, with the result obtained by scalar correction $\delta\mathrm{h}_c$. One can derive from the scalar Born series theory:

$$\delta\mathrm{h}_c = \delta\mathrm{h}_1 \underbrace{\frac{1}{1 + \frac{\delta\mathrm{h}_1}{2}}}_{\text{scalar correction}} . \tag{28}$$

C. Radial compensation

The ultrasonic beam generated by the transducer has a finite aperture angle. This implies the radial anisotropy phenomenon observed on reconstructed images. The response of the defects depends on their distance from the image center. To take into account this phenomenon, it is necessary to perform a radial gain compensation (RGC). We were not able to perform the radial calibration experimentally. A first estimate of the radial decrease law can be deduced from the field calculated by FEM, exposed previously. However, we observed a more significant decrease by comparing, *a posteriori*, the reconstructed thicknesses with the real defects. We will take this issue into account in the analysis of the results. The estimated radial decrease laws are given in figure 7.

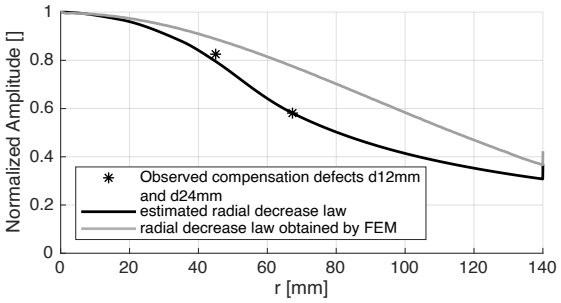

FIG. 7. Estimation of the radial decrease law for the case of reflection mode tomography: comparison of FEM field computation, *a posteriori* correction.

IV. EXTINCTION MODE METHODOLOGY

A. Experimental setup

The extinction mode tomography experiments on the phantom were carried out in immersion. The advantage of the immersion configuration is the coupling homogeneity. One can note that this immersion configuration is difficult to apply to the reflection mode tomography, because of the insonification of the water around the disk, involving interfering reflections whose amplitude is greater than the information coming from the disk. Nevertheless, in transmission mode, the speed in the disk being much higher than the speed in water, the information coming from the propagation in the disk is separated from that coming from the propagation in water. The disk was suspended using a nylon thread assembly, so that the disk underwent only slight mechanical stress. The adjustment of the position of the disk (inclination, centering) was made manually. Therefore, we expected deviations in the homogeneity (axisymmetry) of the insonification of the disk. The transmission aperture considered, associated with the angle γ, was 90 degrees, and was divided into 37 positions. The number of insonification angles was 32, that is, an angular step in θ of 11.25 degrees. We used two pairs of IMASONIC $^{\text{TM}}$ transducers with cylindrical focusing at 150 mm, aperture 56 mm, frequency 500 kHz and 1 MHz, respectively, placed 150 mm from the edge of the disk. A photograph of the experimental configuration is given in figure 8.

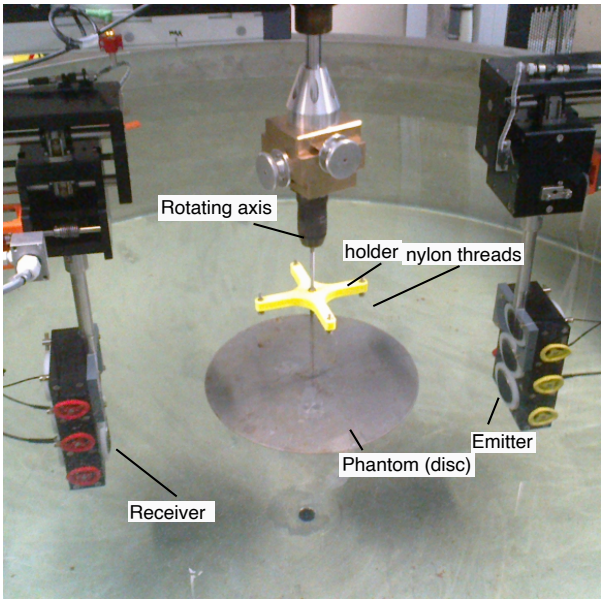

FIG. 8. Photograph of the extinction mode tomography experimental setup.

B. Reconstruction algorithm

The data consisted in measuring for each position (θ, γ) the extinction of the echo transmitted compared with the echo measured in the case of the healthy disk. The acquisition on the healthy disk made it possible to measure the reference beam divergence law in amplitude and time-of-flight. Theoretical rays were calculated by applying Snell-Descartes law to the disk-water interface ($c_M = 5380$ m/s, $c_0 = 1480$ m/s), for rays starting from the center of the emitting transducer. A first rough reconstruction consists in using the ray density functions in the parameterization (θ, γ). This representation is in some cases useful to get a quick view of the location of the defects. The application of the filtered back projection (FBP) requires the transformation of this parameterization towards the Radon parameterization (r, θ), where r is the distance of the ray to the center. The transformation includes redundancies and sampling gaps inherent in the well-known fan-beam configuration. We made

sure that the transformation did not alter the data by using an interpolation and averaging method. The results provide an image of the extinction power of the defects.

V. REFLECTION MODE RESULTS

The raw reflection sinogram is given in figure 9a, in saturated scale. The echoes coming from the defects are distinguishable from the excitation dead zone and the bottom echo. In order to obtain a result independent of the echoes that do not carry information about the defects, we manually filtered those echoes, to obtain a filtered sinogram. Please note that one can assume that this filtering operation could be done physically by using a delay line to separate echoes, or automatically using an algorithm. The deconvolved sinogram, after application of the method presented previously, is given in figure 9b. The choice of parameters resulted from a trade-off between the sparse representation of the consistent part of the sinogram and the noise filtering. Note the compensation of the excitation delay of about 4.2 μs, necessary for the consistent localization of the defects.

The results of the reflection mode tomography of the phantom are exposed as follows. The result of adjoint tomography obtained by the superposition of 72 thickness perturbation kernels is given in figure 10. The conventional qualitative Radon filtered backpropagation (FBP) of the envelope of the gated raw sinogram is shown in figure 11. The qualitative images are given in linear scale, adjusted according to the min and max. The first secant result applied to first Born quantitative reconstruction, including radial gain compensation, is given in figure 12. Figure 13 gives a comparison between first Born image, first secant image and contrast correction image, for both cases with and without radial gain compensation.

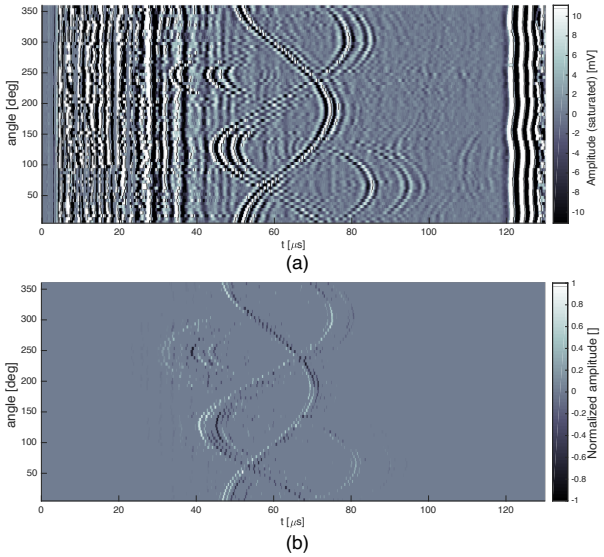

FIG. 9. Measured sinograms: (a) Raw reflection sinogram, in saturated scale, (b) Deconvolved sinogram using gradient descent algorithm, with l_1-norm penalization.

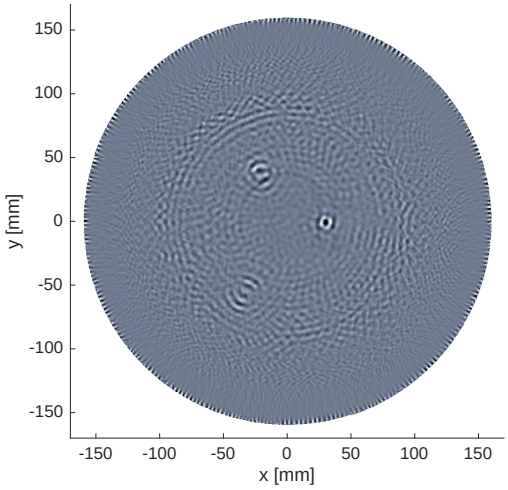

FIG. 10. Reflection mode adjoint field tomography, qualitative reconstruction using thickness perturbation kernel superposition.

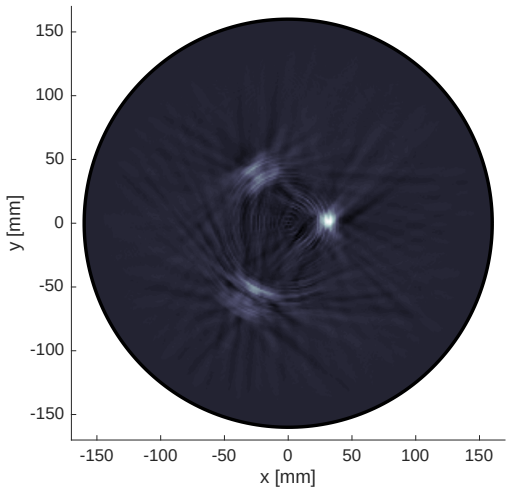

FIG. 11. Reflection mode conventional Radon FBP qualitative tomography, without deconvolution.

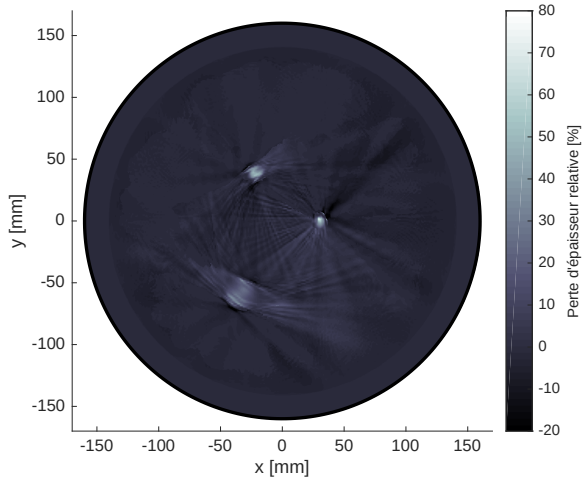

FIG. 12. Reflection mode first secant quantitative thickness reconstruction, using deconvolution and radial gain compensation.

VI. EXTINCTION MODE RESULTS

The results of the extinction mode tomography of the phantom are exposed by comparing the results obtained for the two frequencies 500 kHz and 1 MHz. The measured extinction

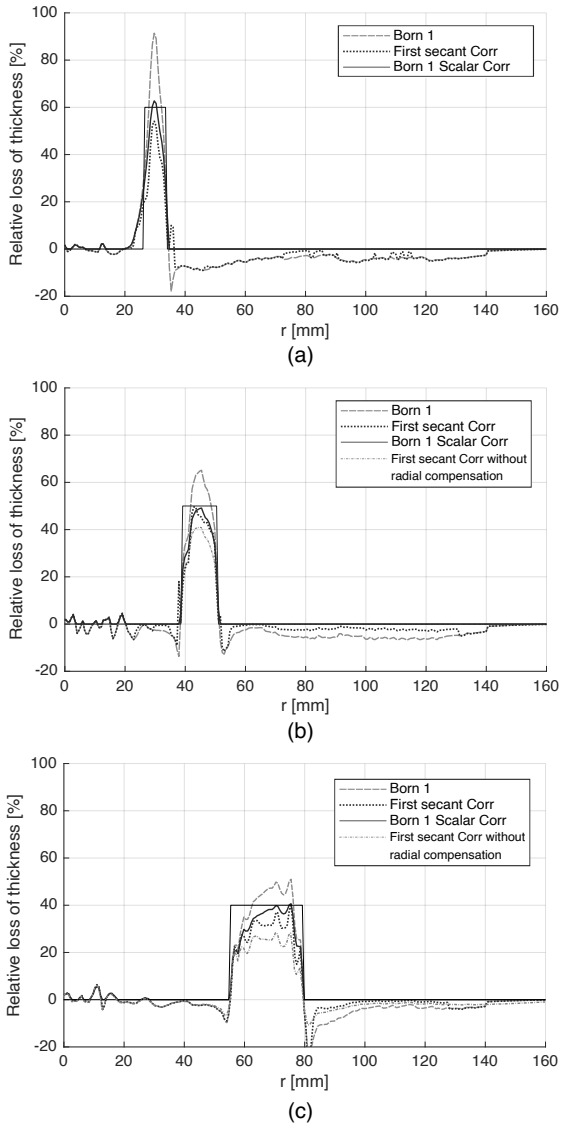

FIG. 13. Comparison of cross sections along defects for different images : first Born reconstruction (Born 1), first secant correction (First secant Corr), first Born reconstruction with scalar correction (Born 1 scalar Corr): (a) defect 8 mm depth 60 % axis ($\theta = 0°$), (b) defect 12 mm depth 50 % axis ($\theta = 120°$), (c) defect 24 mm depth 40 % axis ($\theta = 240°$). Comparison with the actual profile of defect (rectangular profile).

sinograms are given in appendix C in figure 18. The sinogram in figure 18a shows the

representation of the geometry of the defects in the fan-beam parametrization (θ, γ). The fan-beam filtered backprojection results are given in figure 14.

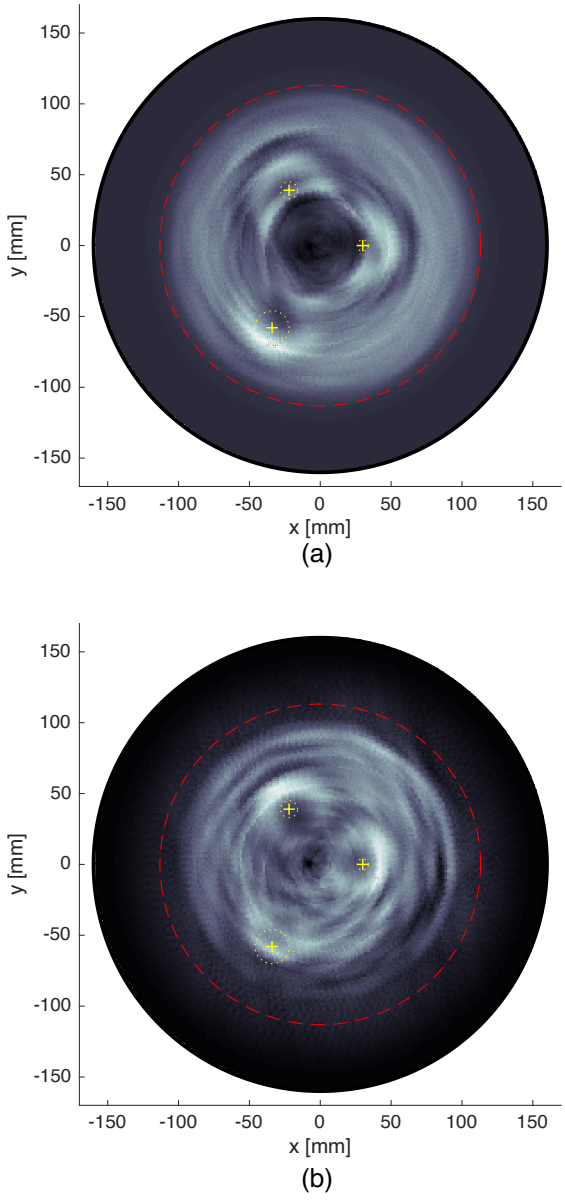

FIG. 14. Extinction mode tomography using qualitative FBP Radon reconstruction. The dashed line denotes the limit of complete sampling due to limited fan-beam aperture angle. The crosses denote the centers of the defects: (a) 500 kHz, (b) 1MHz.

VII. DISCUSSION

A. Reflection mode

The fit of the FEM model makes it possible to obtain a good localization of the defects using the thickness perturbation kernel superposition (fig. 10). The qualitative FBP reconstruction is consistent with the contours of the defects (fig. 11). We observe on these two reconstructions the phenomenon of spatial undersampling for the 12 mm and 24 mm defects. As expected, the two methods, which are different in nature but consist of backpropagation of raw echos without deconvolution, give comparable results in terms of detection and resolution.

Deconvolution allows a gain in resolution and defect localization. The gain in resolution is notably observable on the 8 mm defect. The result is very sensitive to the deconvolution parameters. It has to be noted that the method used, based on the sparse representation of the signals and on a low-pass filter depending on the size and the regularity of the defects, is valid for a non-dispersive and non-diffusive homogeneous medium, and for defects relatively localized in space.

The scalar contrast correction result is close to the first secant correction result, see fig. 13a. For computational cost reasons, it may not be interesting to compute the first secant, which requires the computation of the full direct problem for each insonification angle. Part of the defect diffraction has got an SH component, see *e.g.* directivity diagrams in fig. 4. We therefore expect the scalar reconstruction to be undersized compared with the $S-SH$ vector reconstruction. Comparison between scalar correction and first secant correction, see

figures 13b and 13c, shows that this undersizing effect is not significantly observed. We can conclude that the "vectorial" mode conversion effects $S \leftrightarrow SH$, involved in the first secant reconstruction, are negligible.

The 12 mm defect and especially the 24 mm defect are undersized, in terms of depth. The coupling inhomogeneity has a significant influence on the amplitude of the measured signals. Theoretically, the application of radial gain compensation makes it possible to overcome the undersizing effect. The negative consequence of the RGC is the presence of reconstruction artifacts, whose amplitude increases with the distance to the center (by non-homogeneity of the Radon sampling). Consequently, when solving the direct problem on the reconstructed thickness map, the artifacts may have a diffracting effect that does not correspond to the real defect, which can bias the result.

a. Selection of the method and instrumentation. The method of S_0 mode excitation on the edge of the plate is relevant in the membrane regime. The quality of the signals is determined by the coupling on the edge of the plate. This mode of excitation requires the design of a suitable coupling system. The SNR obtained on the phantom studied is sufficient to allow good reconstruction of the defects. The *a priori* method exposed in section 2 made it possible to estimate the response of the defects according to three parameters: regularity, depth and characteristic size. The method provides information on the detectability of defects. In the case of regular and shallow defects, one can expect detection limitations.

B. Extinction mode

Relatively good defect detection is obtained from the extinction data. The extinction phenomenon is very sensitive to the frequency and depth of the defect, as shown on the extinction diagram in figure 2(b). The location of defects on the images is globally consistent with the actual positions. We can assert that there is no significant gain in detection at 1 MHz. This agrees with predictions we also made at 1 MHz. The defect size amplification error is due to the aperture of the extinction lobe, observable in fig. 4. Extinction tomography is generally applied in the geometric/optical regime. In this regime, the extinction lobe is very narrow, which allows extinction ray tomography with low sizing error. In the Mie regime, the extinction lobe is wider. Nevertheless, it is possible to localize the center of each defect by taking this bias into account.

Extinction data due to the disk position offset is observable on the sinogram in fig. 18(b). Part of the inconsistent extinction can be expected to be due to the non-coincidence of the focal plane of the transducers with the plane of the plate, although we tried to minimize this error. This adjustment, which is relatively sensitive, was made manually.

Because of the nature of the fan-beam configuration, the image reconstruction area is reduced to an area near the center, determined by the beam width. This can be a limitation in the case of defects far from the center.

VIII. CONCLUSION

The membrane regime is a good configuration for performing reflection mode and extinction mode tomography of sharp defects in isotropic plates. The method presented was based on an analytical description of plate waves in the fundamental regime. The quantitative method involves the inversion of the direct ultrasonic field by gain compensation (axial and radial), the inversion of the excitation waveform by deconvolution, and the thickness loss calibration from measurements made on calibrated defects. Phenomena and issues specific to tomography applied to plate waves, which determine the performance of detection and resolution, were identified: necessity of homogeneous coupling, extinction lobe aperture, inversion calibration, deconvolution parameters. Conventional FBP Radon reconstruction, in both reflection and extinction mode, allows good defect localization. It would be relevant to make this type of acquisition with a reflection aperture in order to increase the contrast and the sampling. The inversion method selected showed the relevance of post-processing of raw ultrasound signals. Although the method includes manual operations, which include bias, we believe that it is possible to completely automate the inversion via algorithms. The reflection mode and extinction mode are two different ways of getting information about defects. The main interests of extinction tomography are the detection and localization of defects, and the qualitative evaluation of their importance. In a real configuration, extinction mode tomography may be simpler to implement. The results, although restricted to a simple case, help to show the contribution of digital signal processing techniques for NDT applications, particularly in the field of industrial parts and structures.

IX. ACKNOWLEDGMENT

This work was funded by the National Association of Research and Technology (ANRT) and the Technical Center for Mechanical Industry (CETIM).

APPENDIX A:

1. Mode 1 incident

relating ϕ_{inc} to ϕ_{scat}:

$$t_1^1(\mathbf{s},\mathbf{s}_0) = ik_1\mathbf{s}\cdot\frac{k_1^2}{I_0}A_1\int_{\mathbb{R}^2}\nabla\delta I_0(\mathbf{x})e^{ik_1(\mathbf{s}_0-\mathbf{s})\cdot\mathbf{x}}d\mathbf{x}\,, \tag{A1}$$

relating ϕ_{inc} to H_{scat}:

$$t_2^1(\mathbf{s},\mathbf{s}_0) = ik_2\mathbf{s}\times\frac{k_2^2}{I_0}A_2\int_{\mathbb{R}^2}\nabla\delta I_0(\mathbf{x})e^{i(k_1\mathbf{s}_0-k_2\mathbf{s})\cdot\mathbf{x}}d\mathbf{x}\,, \tag{A2}$$

2. Mode 2 incident

relating H_{inc} to ϕ_{scat}:

$$t_1^2(\mathbf{s},\mathbf{s}_0) = ik_1\mathbf{s}\cdot\frac{k_1^2}{I_0}A_1\int_{\mathbb{R}^2}\nabla^\perp\delta I_0(\mathbf{x})e^{i(k_2\mathbf{s}_0-k_1\mathbf{s})\cdot\mathbf{x}}d\mathbf{x}\,, \tag{A3}$$

relating H_{inc} to H_{scat}:

$$t_2^2(\mathbf{s},\mathbf{s}_0) = ik_2\mathbf{s}\times\frac{k_2^2}{I_0}A_2\int_{\mathbb{R}^2}\nabla^\perp\delta I_0(\mathbf{x})e^{ik_2(\mathbf{s}_0-\mathbf{s})\cdot\mathbf{x}}d\mathbf{x}\,, \tag{A4}$$

where the tangential gradient is defined by

$$\nabla^{\perp} := [\partial_y, -\partial_x]^T . \tag{A5}$$

APPENDIX B:

1. Measurement of the acoustic properties of the phantom's material

The disk's material is carbon steel dedicated to stamping. The pressure wave velocity c_L measurement was carried out in the thickness of the disk according to the high frequency method.. The membrane wave velocity c_M measurement was carried out according to a differential method performed in transmission immersion mode at 500 kHz on a 320×320 mm plate of the same material. The measured and deduced values are given in table I.

2. Calibration of deconvolution algorithm

The estimate of the response of S_0 reflection to thickness loss was made by fitting the theoretical reflected echo model, illustrated in fig. 2, to a set of measurements for different depths. We made a 320×320 mm calibration plate containing five defects, diameter 6 mm, depths 20 %, 40 %, 50 %, 60 % and 70 % . The amplitude correction from the case of the square plate to the case of the disk (weaker excitation amplitude due to the curvature of the excited surface) was made with respect to the bottom echo. The results of the thickness loss calibration are given in figure 15.

TABLE I. Measurement of the acoustic properties of the phantom's material.

Parameter	Symbol	Value	Unit
Pressure wave speed	c_L	6098	m/s
Membrane wave speed	c_M	5380	m/s
Density	ρ	7815	kg/m^3
Thickness	h	2	mm
$\Longrightarrow$ Young Modulus	E	203,05	GPa
$\Longrightarrow$ Poisson ratio	ν	0,32	
$\Longrightarrow$ Shear wave speed	c_T	3137	m/s
$\Longrightarrow$ SH_1 cut-off frequency	$f_{c,1}$	778	kHz

The adjustment of the deconvolution parameters is illustrated in figure 16 with the application to the echo of depth 60 %. The result obtained under the axisymmetric hypothesis shows that the 2D reconstruction from the sparse signal gives rise to very strong gradients. As mentioned in the article, the parameters of the LP filter were adjusted relative to the prior knowledge of defect regularity.

3. Fit of FEM model

The material constants of the model were identified with the values of the measurements reported in table I. The source waveform of the model was identified with the measured

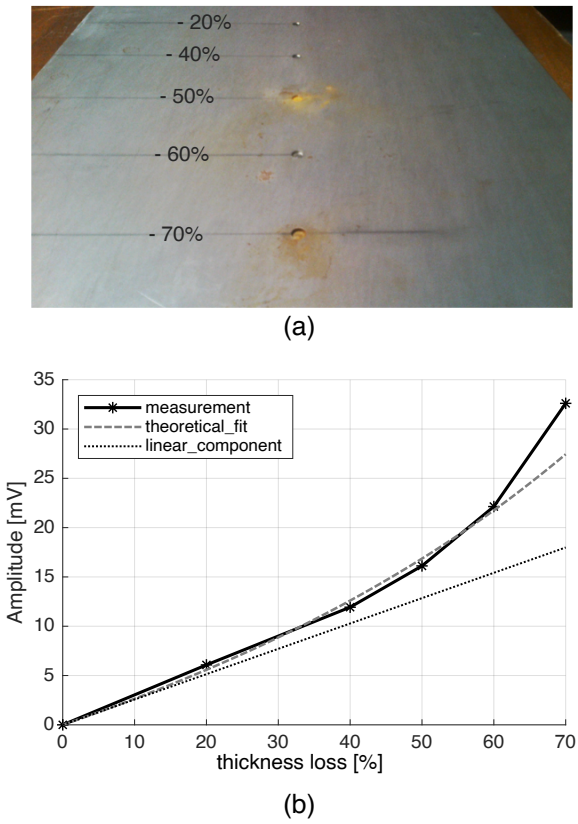

FIG. 15. Measurement and fit of the response of S_0 reflection to thickness loss, for the amplitude calibration of the inverse problem: (a) photograph of the calibration plate containing the defects diameter 6 mm of different depths (b) measured reflection amplitudes.

source, given in figure 6. The direct problem associated with the reflection mode measurement was fit in phase and amplitude relative to the bottom echoes measured on the healthy reference disk. This fit is illustrated in figure 17. Acceptable phase and amplitude consistency is obtained on the bottom echoes. The region of interest (ROI) being a two diameter path of the S_0 wavefront, the secondary echoes were not analyzed. One can note that this model does not take into account displacements out of the plane of the plate, and thus ne-

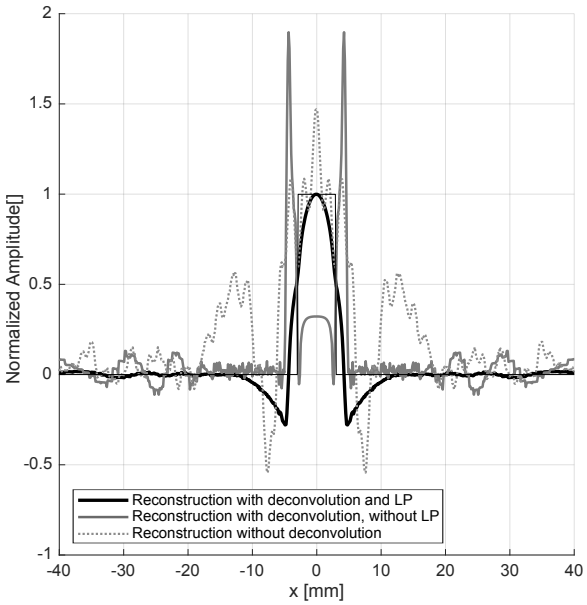

FIG. 16. Application of the deconvolution algorithm to the defect, diameter 6 mm, depth 60%, 2D reconstruction in axisymmetric hypothesis, comparison of cases with or without deconvolution and adjusted low-pass filter (LP).

443 glects A modes and excited higher order modes. Deviations are expected on the secondary
444 echoes.

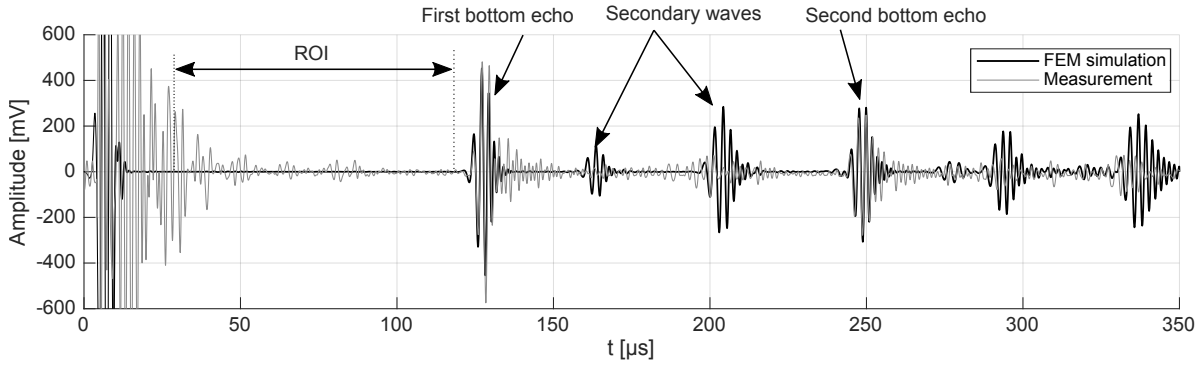

FIG. 17. Illustration of the fit of the FEM model compared with the experimental signal obtained in the case of the healthy disk in reflection.

APPENDIX C:

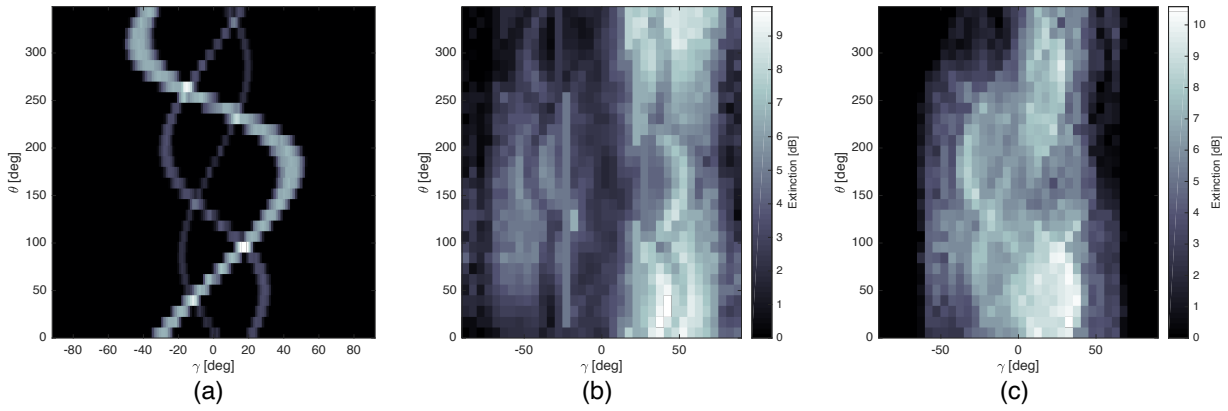

FIG. 18. Sinograms measured in parametrization (θ, γ), comparison with the real positions of the defects: (a) Ideal defect positions, (b) observed 500 kHz, (c) observed 1 MHz.

Albiruni, F., Cho, Y., Lee, J.-H., and Ahn, B.-Y. (**2012**). "Non-contact guided waves tomographic imaging of plate-like structures using a probabilistic algorithm," MATERIALS TRANSACTIONS **53**(2), 330–336, doi: 10.2320/matertrans.I-M2011853.

Bossmann, F., Plonka, G., Peter, T., Nemitz, O., and Schmitte, T. (**2012**). "Sparse Deconvolution Methods for Ultrasonic NDT," Journal of Nondestructive Evaluation **31**(3), 225–244, https://doi.org/10.1007/s10921-012-0138-8, doi: 10.1007/s10921-012-0138-8.

Cailly, W., Walaszek, H., Brzuchacz, S., Fan, Z., and Lasaygues, P. (**2019**). "Low-frequency guided wave quantitative reconstruction of corrosion in plates, 1d diffraction problem," Acta Acustica united with Acustica **105**, 970–986, doi: 10.3813/AAA.919378.

Carcreff, E., Bourguignon, S., Duclos, A., Simon, L., and Idier, J. (**2015**). "Detection of flat bottom holes using sparse deconvolution," Vol. 70, doi: 10.1016/j.phpro.2015.08.019.

Diligent, O., Grahn, T., Bostrom, A., Cawley, P., and Lowe, M. J. S. (**2002**). "The low-frequency reflection and scattering of the S0 Lamb mode from a circular through-thickness hole in a plate: Finite Element, analytical and experimental studies.," The Journal of the Acoustical Society of America **112**(6), 2589–2601.

Diligent, O., Lowe, M. J. S., Cawley, P., and Wilcox, P. (**2003**). "Reflection of the S0 Lamb Mode from a PartDepth Circular Defect in a Plate, When the Incident Wave is Created by a Small Source," AIP Conference Proceedings **657**(1), 197–204, https://aip.scitation.org/doi/abs/10.1063/1.1570137, doi: 10.1063/1.1570137.

Druet, T., Recoquillay, A., Chapuis, B., and Moulin, E. (**2019**). "Passive guided wave tomography for structural health monitoring," The Journal of the Acoustical Society of America **146**(4), 2395–2403, https://doi.org/10.1121/1.5128332, doi: 10.1121/1.5128332.

Huang, S., Zhang, Y., Wang, S., and Zhao, W. (**2016**). "Multi-mode electromagnetic ultrasonic lamb wave tomography imaging for variable-depth defects in metal plates," Sensors **16**(5), 628, doi: 10.3390/s16050628.

Huthwaite, P. (**2014**). "Evaluation of inversion approaches for guided wave thickness mapping," Proceedings of the Royal Society of London A: Mathematical, Physical and Engineering Sciences **470**(2166), http://rspa.royalsocietypublishing.org/content/470/2166/20140063, doi: 10.1098/rspa.2014.0063.

Huthwaite, P., and Simonetti, F. (**2011**). "High-resolution imaging without iteration: a fast and robust method for breast ultrasound tomography," The Journal of the Acoustical

Society of America **130**(3), 1721–1734, https://doi.org/10.1121/1.3613936, doi: 10.1121/1.3613936.

Huthwaite, P., and Simonetti, F. (**2013**). "High-resolution guided wave tomography," Wave Motion **50**(5), 979 – 993, http://www.sciencedirect.com/science/article/pii/S0165212513000759, doi: https://doi.org/10.1016/j.wavemoti.2013.04.004.

Lasaygues, P., and Lefebvre, J.-P. (**2000**). "Deconvolution in low frequency ultrasonic tomography," Acta Acustica united with Acustica **86**(3), 506–514, doi: 10.1007/978-1-4615-4791-4_121.

Liu, Q., and Tromp, J. (**2008**). "Finite-Frequency Sensitivity Kernels for Global Seismic Wave Propagation Based upon Adjoint Methods," Geophysical Journal International **174**(1), 265–286, https://onlinelibrary.wiley.com/doi/abs/10.1111/j.1365-246X.2008.03798.x, doi: 10.1111/j.1365-246X.2008.03798.x.

Lowe, M. J. S., and Diligent, O. (**2002**). "Low-frequency reflection characteristics of the s0 Lamb wave from a rectangular notch in a plate," The Journal of the Acoustical Society of America **111**(1), 64–74, https://doi.org/10.1121/1.1424866, doi: 10.1121/1.1424866.

Mindlin, R. D. (**1951**). "Influence of rotatory inertia and shear on flexural motions of isotropic, elastic plates," ASME Journal of Applied Mechanics **18**, 31–38.

Nonn, S., Schagerl, M., Zhao, Y., Gschossmann, S. and Kralovec, C. (**2018**). "Application of electrical impedance tomography to an anisotropic carbon fiber-reinforced polymer composite laminate for damage localization," Composites Science and Technology **160**(4), 231–236, https://doi.org/10.1016/j.compscitech.2018.03.031, doi:

10.1016/j.compscitech.2018.03.031.

O'Brien, M., Sinclair, T., and Kramer, S. (**1995**). "Recovery of a sparse spike time series by l1 norm deconvolution," Signal Processing, IEEE Transactions on **42**, 3353 – 3365, doi: 10.1109/78.340772.

Reissner, E. (**1945**). "The effect of transverse shear deformation on the bending of elastic plates," ASME Journal of Applied Mechanics **12**, A6877.

Rose, L. R. F., and Wang, C. H. (**2004**). "Mindlin plate theory for damage detection: Source solutions," The Journal of the Acoustical Society of America **116**(1), 154–171, https://doi.org/10.1121/1.1739482, doi: 10.1121/1.1739482.

Soussen, C., Idier, J., Carcreff, E., Simon, L., and Potel, C. (**2012**). "Ultrasonic non destructive testing based on sparse deconvolution," Journal of Physics: Conference Series **353**, 012018, https://doi.org/10.1088-2F1742-6596-2F353-2F1-2F012018, doi: 10.1088/1742-6596/353/1/012018.

Tabatabaeipour, M., Hettler, J., Delrue, S., and Van Den Abeele, K. (**2014**). "Reconstruction Algorithm for Probabilistic Inspection of Damage (RAPID) in Composites," in *European Conference on Non-Destructive Testing 2014*.

Wang, D., Ye, L., Su, Z., Lu, Y., Li, F., and Meng, G. (**2010**). "Probabilistic Damage Identification Based on Correlation Analysis Using Guided Wave Signals in Aluminum Plates," Structural Health Monitoring **9**(2), 133–144, https://doi.org/10.1177/1475921709352145, doi: 10.1177/1475921709352145.

Wang, D., Zhang, W., Wang, X., and Sun, B. (**2016**). "Lamb-Wave-Based Tomographic Imaging Techniques for Hole-Edge Corrosion Monitoring in Plate Structures," Materials

9(11), 916, http://www.ncbi.nlm.nih.gov/pmc/articles/PMC5457213/, doi: 10.3390/ma9110916.

Zala, C. A. (**1992**). "High-resolution inversion of ultrasonic traces," IEEE Transactions on Ultrasonics, Ferroelectrics, and Frequency Control **39**(4), 458–463, doi: 10.1109/58.148535.

Zhao, L., Yang, J., Wang, K.W., and Semperlotti, F. (**2015**). "An application of impedio-graphy to the high sensitivity and high resolution identification of structural damage," Smart Materials and Structures **24**(6), 065044, https://doi.org/10.1088/0964-1726/24/6/065044, doi: 10.1088/0964-1726/24/6/065044.

Zhao, L., and Semperlotti, F. (**2019**). "Detection of breathingtype damage using multi-harmonic electrical impedance tomography," Struct Control Health Monit **26**(4), e2330, https://doi.org/10.1002/stc.2330, doi: 10.1002/stc.2330.